

Optimizing Large Scale Imaging Surveys for a Retrospective Relative Photometric Calibration

R. Holmes¹ and H.-W. Rix¹

Max-Planck-Institut für Astronomie, Königstuhl 17, Heidelberg, 69117, Germany.

and

D. W. Hogg²

² Center for Cosmology and Particle Physics, Department of Physics, New York University,

4 Washington Place, New York, NY 10003, USA.

Received _____; accepted _____

ABSTRACT

In this paper we show that, with due care given to the observing strategy, it will be possible to accurately constrain the relative photometric calibration of instruments used in large imaging surveys with their science data alone. We create end-to-end simulations of an imaging survey, which produces simulated datasets from mock observations of a synthetic sky according to a defined survey strategy. These catalog based simulations include realistic measurement uncertainties and a complex, position dependent instrument response. We then use a self-calibration technique to recover the relative instrument response by fitting an model that best explains the survey dataset, based on the multiple observations of (non-varying) sources at different focal plane positions. By considering four simple survey strategies we find that, with a correct redundancy built into the survey strategy, it is possible to accurately constrain the relative photometric response of an imaging instrument, and therefore the relative calibration of the resulting dataset. The majority of the remaining post self-calibration errors are due to the limitations in the basis used to model the relative instrument response. We find that returning the same sources to very different focal plane positions is the key property of a survey strategy that is required for an accurate calibration. From the results of this work, we are able to highlight an important point for those considering the design of large scale imaging surveys: depart from a regular tiling of the sky and return the same sources to very different focal plane positions.

Subject headings: Relative Photometric Calibration: Imaging Survey: Survey Strategy

1. Introduction

Astronomers tend to think in terms of taking science data and calibration data separately. The former is used for science and the latter is used to constrain instrument parameters, such as the instrument response, the dark currents and so-on. But typically far more photons are collected during science exposures themselves; are these not incredibly constraining on the calibration? Indeed, in the retrospective photometric calibration of the Sloan Digital Sky Survey data (SDSS), much more calibration information was obtained from the science data than the calibration data (Padmanabhan et al. 2008). But, of course, the SDSS imaging strategy had to be adjusted to make this calibration work: good redundancy is required in the data stream, and a redundancy of a very specific kind.

In this paper, we argue that the next generation of large-scale imaging surveys should have their observation strategies optimized from the very start with this kind of “self-calibration” in mind. This work focuses on the relative photometric calibration of a typical imaging instrument only, although we also suspect that similar techniques could be used to constrain many other calibration parameters. The self-calibration technique utilizes the multiple measurements of (non-varying) sources, at different focal plane positions and at different times within the survey, to constrain the relative instrument response by requiring that the post-calibration measurements yield the same flux values. Through end-to-end, catalog level survey simulations¹, we aim to identify the important properties of survey strategies that makes them advantageous for this kind of self-calibration.

We construct realistic survey datasets through mock observations of a synthetic sky according to a specified survey strategy. These simulations include a complex, position dependent instrument response for the imaging instrument. Through the self-calibration

¹All of the code used in this work is publicly available at XX.

procedure, we then recover this instrument response by fitting a model that best describes the survey dataset. By comparing the *fitted* instrument response to the *true* instrument response we are able to assess the performance of the self-calibration procedure with different survey strategies. There is a degeneracy in this problem: the self-calibration procedure is only able to fit for a *relative* instrument response. We have no way to know, for example, if all the sources are uniformly fainter, or if the instrument sensitivity is uniformly lower.

In Section 2 we introduce the simulation chain constructed to produce the realistic survey datasets. Section 3 goes onto to detail the self-calibration procedure. In Section 5 we focus on four simple survey strategies, which allow us to draw conclusions on the performance of the self-calibration procedure with different survey properties. We do not produced pixelated images; instead we concentrate on catalog level simulations with realistic measurement uncertainties. Complex effects are included in the simulations that are not precisely modeled at the analysis stage, in order to simulate the effects of unknown systematic errors within the dataset.

2. Survey Dataset Simulations

We have constructed an end-to-end simulation chain that produces a realistic imaging dataset from a specified survey strategy. In this work we have kept the simulation parameters intentionally flexible, so that the sensitivity of the self-calibration procedure to different values can be investigated. The simulations are split into a number of steps. The first of which is the generation of a synthetic sky. With a given pointing, single mock observations are performed on this sky. To build up a survey wide dataset, multiple single observations are performed according to the specified survey strategy. In this section, we detail the assumptions and methods used in each of these steps.

2.1. The Synthetic Sky

We generate a representative synthetic sky based on realistic object densities in the AB magnitude range $m_{\min} = 17$ to $m_{\max} = 22$ mag_{AB}, with these limits chosen to be consistent with the saturation and 10σ limits of deep, space-based, near-infrared survey. Sources are generated with random coordinates (uniformly distributed within the sky region being investigated) and with random magnitudes m distributed according to

$$\log_{10} \frac{dN}{dm d\Omega} = a + b m + c m^2 \quad , \quad (1)$$

where $\frac{dN}{dm d\Omega}$ is the density of sources N per unit magnitude m and per unit solid angle Ω , and a , b and c are model parameters. Even though our simulations make no distinction between galaxies and stars, the values of the parameters are found from fitting the Y-band galaxy populations reported in (Windhorst et al. 2011) only. These parameters were found to be $a = -13.05$, $b = 1.25$ and $c = -0.02$. We intentionally omit the stellar population, so that the conclusions drawn from these simulations are independent of the final position of the survey area on the sky. The source magnitudes m are related to the source fluxes s simply by: $m = 22.5 - 2.5 \log_{10}(s)$, where the 22.5 puts the fluxes in units of nanomaggies (nmgy). Due to computational reasons, we only select the brightest sources within the survey area, up to a source density d , for the self-calibration procedure.

2.2. A Single Exposure

With a camera pointing (α, β) and camera orientation θ this synthetic sky is transformed into focal plane image. In our simulations, we use a large instrument field-of-view of $0.76 \text{ deg} \times 0.72 \text{ deg}$; a size consistent with the next generation of large survey imagers. An example of a single pointing exposure is shown in Figure 1.

2.2.1. Measured Count Rates

We do not consider pixelated images in these simulations; instead the true source fluxes s_{true} are converted into measured count rates c with an complex, position dependent instrument response model f_{true} and a measurement noise model. For a measurement i the count rate c_i recorded from a source k depends on the *true* instrument response $f_{\text{true}}(\vec{x}_i|\vec{q}_{\text{true}})$, which is a function of focal plane position \vec{x}_i , and the source's true flux $s_{k,\text{true}}$

$$c_i = f_{\text{true}}(\vec{x}_i|\vec{q}_{\text{true}}) s_{k,\text{true}} + e_i \quad ,$$

where \vec{q}_{true} are the parameters defining the *true* instrument response, and e_i is a noise contribution drawn from the Normal Distribution $N(e|0, \sigma_{\text{true}}^2)$.

2.2.2. Noise Model

To construct the noise model, the simulated exposures are assumed to be background limited and that, for systematic reasons, there is an upper limit on the signal-to-noise ratio of 500 for bright sources. The noise model is complicated further by applying an extra term ϵ_i to the count rates' uncertainty variance, which we intentionally do not take into account in the analysis in order to simulate systematic problems with the instrument noise model. The *true* noise model is therefore

$$\sigma_{i,\text{true}}^2 = (1 + \epsilon_i) \alpha^2 + \eta^2 [f_{\text{true}}(\vec{x}_i|\vec{q}_{\text{true}}) s_{k,\text{true}}]^2 \quad , \quad (2)$$

where α and η are both constants and ϵ_i is a random number, in the range $[0.0, \epsilon_{\text{max}})$, generated for each measurement i . The $m = 22$ mag 10σ detection limit introduced previously and the 500 limit on the signal-to-noise ratio are used to set $\alpha = 0.1585$ and $\eta = 0.0017$. The ϵ_i contribution is not taken into account in the analysis and therefore the uncertainty variances on the count rates are assumed to be

$$\sigma_i^2 = \alpha^2 + \eta^2 c_i^2$$

during this stage.

2.2.3. The True Instrument Response Model

We construct a complex, position independent instrument response model $f_{\text{true}}(\vec{x}_i|\vec{q}_{\text{true}})$ from a superposition of large and small-scale variations:

$$f_{\text{true}}(\vec{x}_i|\vec{q}_{\text{true},1\dots260}) = f_{\text{large}}(\vec{x}_i|\vec{q}_{\text{true},1\dots6}) + f_{\text{small}}(\vec{x}_i|\vec{q}_{\text{true},7\dots260}) \quad ,$$

where $\vec{x}_i = (x_i, y_i)$ is the focal plane position that the k th source falls at during the i^{th} measurement and \vec{q}_{true} are the parameters defining the instrument response model. The large-scale instrument response $f_{\text{large}}(\vec{x}_i|\vec{q}_{\text{true},1\dots6})$ is modeled as a second order polynomial:

$$f_{\text{large}}(\vec{x}_i|\vec{q}_{\text{true},1\dots6}) = q_{\text{true},1} + q_{\text{true},2} x_i + q_{\text{true},3} y_i + q_{\text{true},4} x_i^2 + q_{\text{true},5} x_i y_i + q_{\text{true},6} y_i^2 \quad .$$

The small-scale instrument response, which is constructed from sine and cosine contributions, is superimposed on this large-scale instrument response. The small-scale instrument response $f_{\text{small}}(\vec{x}_i|\vec{q}_{\text{true},7\dots260})$ is modeled as

$$\begin{aligned} f_{\text{small}}(\vec{x}_i|\vec{q}_{\text{true},7\dots260}) &= \sum_{a=0}^6 \sum_{b=0}^a [q_{\text{true},7+4b} \cos(k_x x_i) + q_{\text{true},8+4b} \sin(k_x x_i)] \\ &\quad \times [q_{\text{true},9+4b} \cos(k_y y_i) + q_{\text{true},10+4b} \sin(k_y y_i)] \quad , \end{aligned}$$

where

$$\begin{aligned} k_x &= \frac{a \pi}{X} \quad , \\ k_y &= \frac{b \pi}{Y} \quad , \end{aligned}$$

with the physical focal plane dimensions X and Y . In total, the instrument response model is parameterized with 260 parameters; an example can be seen in Figure 1 (right). It is this instrument response that we try and recover with the self-calibration procedure. Our final assumption in these simulations is that the instrument response is temporally stable.

2.3. The Complete Survey

In this work we are interested in simulating complete surveys, in order to identify the crucial characteristics of survey strategies that allow for the relative instrument response model to be accurately, retrospectively constrained from the resulting dataset. We therefore apply the single exposure procedure introduced in the previous section for each pointing specified in a defined survey strategy. The resultant source measurements are collaged into a survey wide dataset.

3. Self-Calibrating the Survey Wide Dataset

We self-calibrate the dataset generated in the survey simulations to recover the true instrument response applied and the true source fluxes. This self-calibration procedure has been successfully applied to ground based imaging surveys, such as the Sloan Digital Sky Survey (Padmanabhan et al. 2008)². This iterative procedure comprises two steps: (1) a refinement of the source flux estimates based on the latest instrument response model and (2) a refinement of the instrument response model based on the updated source flux estimates. These steps are iterated until the system converges, or until it is clear that the system will not converge. There is a degeneracy in the problem, as both the true instrument response and the true source magnitudes are unknown. It is therefore only possible to calibrate the *relative* instrument response and the *relative* source fluxes. It is not possible to know, for example, if the sources are all fainter or if the instrument response is uniformly lower. In practice, this degeneracy can be broken through observations of standard absolute sources.

²Here this procedure is dubbed “uber-calibration.”

3.1. Fitted Measurement Model

To complicate the simulations, we use the self-calibration procedure to fit a model that is *incomplete* in two ways. Firstly, the *fitted* instrument response is modeled as an eighth order polynomial, and not the second order polynomial superimposed with sine and cosine contributions used to model the *true* instrument response. Secondly, the assumed measurement uncertainty variances do not include the additional random measurement error ϵ_i introduced in Subsection 2.2.2. The incomplete measurement model is

$$c_i = f(\vec{x}_i|\vec{q}) s_k + e_i \quad ,$$

where c_i is the recorded count rate, $f(\vec{x}_i|\vec{q})$ is the fitted instrument response model at a focal plane position \vec{x}_i , \vec{q} is a vector parameterizing the eighth order polynomial instrument response model, s_k is the model source flux estimate and the error e_i is drawn from the Normal Distribution $N(e|0, \sigma_i^2)$, such that

$$\sigma_i^2 = \alpha^2 + \eta^2 c_i^2 \quad ,$$

where α and η are the parameters set by the instruments 10σ and saturation limits. The ϵ_i error contribution is intentionally not included in order to simulate systematic problems with the instrument noise model.

3.2. Step 1: Source Flux Refinement

The sources are considered individually in the first step of the self-calibration procedure; their flux estimates are refined based on the latest fitted instrument response parameters \vec{q} . An error function χ_k^2 for all the measurements i of a source k ($i \in \mathcal{O}(k)$) is constructed:

$$\chi_k^2 = \sum_{i \in \mathcal{O}(k)} \frac{(c_i - f_i(\vec{x}_i|\vec{q}) s_k)^2}{\sigma_i^2} \quad ,$$

where c_i are the measured count rates, $f(\vec{x}_i|\vec{q})$ is the fitted instrument response model at a focal plane position \vec{x}_i and σ_i is the assumed noise model. A new estimate of the model source flux s'_k is then found by minimizing the error function with respect to the old model source flux s_k :

$$\frac{d\chi_k^2}{ds_k} = \sum_{i \in \mathcal{O}(k)} \frac{-2f_i(\vec{x}_i|\vec{q})(c_i - f_i(\vec{x}_i|\vec{q})s'_k)}{\sigma_i^2} = 0 \quad ,$$

$$s'_k \leftarrow \left[\sum_{i \in \mathcal{O}(k)} \frac{f_i(\vec{x}_i|\vec{q})^2}{\sigma_i^2} \right]^{-1} \left[\sum_{i \in \mathcal{O}(k)} \frac{f_i(\vec{x}_i|\vec{q})c_i}{\sigma_i^2} \right] \quad .$$

The standard uncertainty variance on the new source flux estimate s'_k is given by

$$\sigma_k'^2 = \left[\sum_{i \in \mathcal{O}(k)} \frac{f_i(\vec{x}_i|\vec{q})^2}{\sigma_i^2} \right]^{-1} \quad .$$

3.3. Step 2: Instrument Response Refinement

The instrument response parameters can now be refined with the latest source flux estimates. A error function for all the measurements of all the sources is constructed

$$\chi^2 = \sum_k \chi_k'^2 \quad ,$$

where

$$\chi_k'^2 = \sum_{i \in \mathcal{O}(k)} \frac{(c_i - f_i(\vec{x}_i|\vec{q})s'_k)^2}{\sigma_i^2} \quad .$$

Recall that the fitted instrument response $f_i(\vec{x}_i|\vec{q})$ is modeled as an eight order polynomial. This can be expressed as

$$f_i(\vec{x}_i|\vec{q}) = \sum_{l=1}^L q_l g_l(\vec{x}_i) \quad ,$$

where $L = 45$ in this case. The total error function χ^2 can be rewritten as

$$\chi^2 = \sum_k \sum_{i \in \mathcal{O}(k)} \frac{(c_i - s'_k \sum_{l=1}^L q_l g_l(\vec{x}_i))^2}{\sigma_i^2} \quad .$$

To refine the instrument response model fit, this error function is minimized with respect to the instrument response model parameters q_l

$$\frac{d\chi^2}{dq_l} = \sum_k \sum_{i \in \mathcal{O}(k)} \frac{-2g_l(\vec{x}_i)s'_k(c_i - s'_k \sum_{l'=1}^{L'} q_{l'} g_{l'}(\vec{x}_i))}{\sigma_i^2} = 0 \quad ,$$

$$\sum_k \sum_{i \in \mathcal{O}(k)} \frac{g_l(\vec{x}_i)s'_k c_i}{\sigma_i^2} = \sum_k \sum_{i \in \mathcal{O}(k)} \frac{g_l(\vec{x}_i)s_k'^2 \sum_{l'=1}^{L'} q_{l'} g_{l'}(\vec{x}_i)}{\sigma_i^2} \quad .$$

It is now simpler to proceed in matrix notation. The following substitutions can be made

$$b_l = \sum_k \sum_{i \in \mathcal{O}(k)} \frac{g_l(\vec{x}_i)s'_k c_i}{\sigma_i^2} \quad , \tag{3}$$

$$G_{ll'} = \sum_k \sum_{i \in \mathcal{O}(k)} \frac{s_k'^2}{\sigma_i^2} g_l(x_i) g_{l'}(x_i) \quad . \tag{4}$$

The matrix equation is then

$$\vec{b} = G \cdot \vec{q'} \quad .$$

The refined instrument response parameters are then found by

$$\vec{q'} \leftarrow G^{-1} \cdot \vec{b} \quad .$$

These two steps are iterated until the solution converges to a final fit of the instrument response $f_{\text{fit}}(\vec{x}|\vec{q}_{\text{fit}})$ and the source fluxes $s_{k,\text{fit}}$, or until it is clear that a solution will not be found.

4. Metrics

To assess the performance of the self-calibration procedure with different survey strategies, it is necessary to quantify the quality of the final fitted solution. To do this we

defined three quantities. The first is the root-mean-squared (RMS) error S_{RMS} in the final fitted source fluxes $s_{k,\text{fit}}$ compared to the true source fluxes $s_{k,\text{true}}$ for the K sources used in the self-calibration procedure:

$$S_{\text{RMS}} = \sqrt{\frac{1}{K} \sum_k^K \left(\frac{s_{k,\text{fit}} - s_{k,\text{true}}}{s_{k,\text{true}}} \right)^2} . \quad (5)$$

The other two metrics, called “badnesses”, are defined as the RMS error between the final fitted instrument response and a reference instrument response sampled on a regular 300×300 grid across the focal plane. For the “True Badness” B_{true} , the *fitted* instrument response $f_{\text{fit}}(\vec{x}|\vec{q}_{\text{fit}})$ is compared to the *true* instrument response $f_{\text{true}}(\vec{x}|\vec{q}_{\text{true}})$ at the J sample points

$$B_{\text{true}} = \sqrt{\frac{1}{J} \sum_j^J \left(\frac{f_{\text{fit}}(\vec{x}_j|\vec{q}_{\text{fit}}) - f_{\text{true}}(\vec{x}_j|\vec{q}_{\text{true}})}{f_{\text{true}}(\vec{x}_j|\vec{q}_{\text{true}})} \right)^2} . \quad (6)$$

The “Best-in-Basis Badness” B_{best} compares the *fitted* instrument response $f_{\text{fit}}(\vec{x}_j|\vec{q}_{\text{fit}})$ to the *best instrument response fit possible* $f_{\text{best}}(\vec{x}_j|\vec{q}_{\text{best}})$ with the basis used to describe the fitted model (in this case an eight order polynomial) at the J sample points

$$B_{\text{best}} = \sqrt{\frac{1}{J} \sum_j^J \left(\frac{f_{\text{fit}}(\vec{x}_j|\vec{q}_{\text{fit}}) - f_{\text{best}}(\vec{x}_j|\vec{q}_{\text{best}})}{f_{\text{best}}(\vec{x}_j|\vec{q}_{\text{best}})} \right)^2} . \quad (7)$$

The badnesses provide a more complete description of the self-calibration performance than the RMS error on the fitted sources’ fluxes, as the RMS source error only applies to the bright sources within the survey selected for the self-calibration procedure.

5. Simple Survey Strategies

In this paper, we consider four simple but very different survey strategies. We use the end-to-end dataset simulation and self-calibration chain, introduced in Sections 2 and 3, to evaluate the performance of the self-calibration procedure with these strategies.

5.1. Survey Description

We label the four survey strategies – which all cover the same patch of sky – with the letters A to D. These survey strategies are summarized in Table 2 and are shown in Figure 2. Strategy A is the simplest strategy; the field is regularly tiled with small overlaps between adjacent pointings ($\sim 5\%$ and $\sim 8\%$ in the camera pointing directions α and β respectively). The pointings in the 12 passes over the same field are exactly aligned. Survey B is the same as A, but with each pass over the field the orientation of the telescope is rotated by 30° . Survey C is more complex. The first pass over the field is the same as in Survey A, with 12×12 pointings. In the next pass, one of the pointings in the α direction is removed and one is added in the β and the pointings are respaced uniformly, so the resultant pointing grid is 13×11 . In the third pass over the field this change is reversed and the field is measured on a 11×13 grid. These three passes are then repeated four times. The pointing positions in Survey D are quasi-random: the pointings are the same as with Survey A, but each has a random offset within $[-0.35, 0.35]$ deg applied in both the α and β directions. By fixing the pointings within these $0.7 \text{ deg} \times 0.7 \text{ deg}$ boxes, we ensure that the quasi random strategy has a uniform coverage of the field. The orientations of the pointings in Survey D are completely random.

5.2. Self-Calibration Performance

The iterative self-calibration procedure converges to a final fitted solution for the Survey B, C and D datasets. With the Survey A dataset it does not converge, even when the system is started close to the optimum fit. The fitted instrument response solutions for the Surveys A to D datasets are shown in Figures 3 to 6. In these plots the final fitted instrument response $f_{\text{fit}}(\vec{x}_j | \vec{q}_{\text{fit}})$ is compared to the true instrument response $f_{\text{true}}(\vec{x} | \vec{q}_{\text{true}})$ and to the best possible instrument response fit with the basis used $f_{\text{best}}(\vec{x}_j | \vec{q}_{\text{best}})$ (“best-in-basis”).

The accuracy of the final fitted solutions are summarized, with the metrics introduced in Section 4, for each of the Survey strategies in Table 3.

FROM HERE NEEDS TO BE UPDATED

The self-calibration procedure performs best with the Survey D dataset, followed by the Survey C dataset, then the Survey B dataset. The self-calibration procedure failed completely with the Survey A dataset and no solution was obtained. With the Survey C and D datasets, the instrument response is accurately recovered. As can be seen from Figs. 5 and 6 (top) the fitted instrument response $f_{\text{fit}}(\vec{x}_j | \vec{q}_{\text{fit}})$ does not perfectly reproduce the true instrument response $f_{\text{true}}(\vec{x} | \vec{q}_{\text{true}})$, with residuals up to the ± 1 % level. That said, through comparisons with the best fit possible with the eight order polynomial basis used in the self-calibration procedure $f_{\text{best}}(\vec{x}_j | \vec{q}_{\text{best}})$ (bottom), we find that majority of the remaining errors are due to limitations in the basis used; the residuals in this comparison are very low and this can be clearly seen in the factor of ~ 10 improvement in the Best-in-Basis Badness B_{best} compared to the True Badness B_{true} .

when the fitted instrument response is compared to the best fit possible with the eight order polynomial basis used in the self-calibration procedure $f_{\text{best}}(\vec{x}_j | \vec{q}_{\text{best}})$ (bottom), we can see that the final solution is close

possible instrument response fit with the basis used $f_{\text{best}}(\vec{x}_j | \vec{q}_{\text{best}})$

The difference between the success of the self-calibration procedure with these four survey strategies is clear: with Surveys A no solution can be obtained, but with the Surveys B, C and D datasets the self-calibration procedure converges close to the correct solution. With the Survey C and D datasets the instrument response can be accurately fitted, close to the best fit possible with the basis used. The majority of the remaining errors in the fit come from the limitations of the basis used in the instrument response model. The

calibration procedure with the Survey B dataset requires more iteration steps (4270) to converge to a final solution, and is less accurate than those found with the Survey C and D datasets, which require 28 and 10 iteration steps respectively.

The results from this investigation into simple survey strategies can be used to draw conclusions about the properties of surveys that make them good, or bad, for retrospective self-calibration. From these examples, I conclude that regular survey strategies with little overlap between adjacent pointings (Survey A) – such as the Euclid Wide Survey – do not allow for the resulting dataset to be self-calibrated effectively. It is therefore necessary to depart from the standard, regularly tiled observing strategies in the Euclid Deep Field. The two best survey strategies (C, D) both return the same sources to very different focal plane positions, and this is the key property which makes their datasets good for self-calibration. By doing so, many different focal plane positions are connected to each other with observations of the same source. This result must be considered when the Deep Field survey strategy is defined and as such I have applied calibration requirements that capture this on the strategy (see Subsection ??). In addition, I also conclude that if the correct redundancy is built into the survey strategy, the self-calibration procedure will be able to accurately constrain the relative instrument response, and therefore the Deep Field relative photometric calibration could be transferred effectively to the Wide Survey. The majority of the remaining errors will come from the limitations of the basis used to fit the instrument response model.

6. Discussion

In this paper, we have considered the optimization of survey strategies for calibrating the relative photometric response of an instrument, but we feel there are many more calibration parameters that can be constrained for this method. For example, the optical

distortion of an instrument could also be constrained with such a method, although we concede that the properties of a survey strategy that makes them good for one calibration, may not be the same as that for another; ultimately a trade-off would need to be performed.

7. Acknowledgments

We are grateful to

REFERENCES

- Padmanabhan, N., Schlegel, D. J., Finkbeiner, D. P., Barentine, J. C., Blanton, M. R., Brewington, H. J., Gunn, J. E., Harvanek, M., Hogg, D. W., Ivezić, Ž., Johnston, D., Kent, S. M., Kleinman, S. J., Knapp, G. R., Krzesinski, J., Long, D., Neilsen, Jr., E. H., Nitta, A., Loomis, C., Lupton, R. H., Roweis, S., Snedden, S. A., Strauss, M. A., & Tucker, D. L., An Improved Photometric Calibration of the Sloan Digital Sky Survey Imaging Data, 2008, ApJ, 674, 1217
- Windhorst, R. A., Cohen, S. H., Hathi, N. P., McCarthy, P. J., Ryan, Jr., R. E., Yan, H., Baldry, I. K., Driver, S. P., Frogel, J. A., Hill, D. T., Kelvin, L. S., Koekemoer, A. M., Mechtley, M., O’Connell, R. W., Robotham, A. S. G., Rutkowski, M. J., Seibert, M., Straughn, A. N., Tuffs, R. J., Balick, B., Bond, H. E., Bushouse, H., Calzetti, D., Crockett, M., Disney, M. J., Dopita, M. A., Hall, D. N. B., Holtzman, J. A., Kaviraj, S., Kimble, R. A., MacKenty, J. W., Mutchler, M., Paresce, F., Saha, A., Silk, J. I., Trauger, J. T., Walker, A. R., Whitmore, B. C., Young, E. T., The Hubble Space Telescope Wide Field Camera 3 Early Release Science Data: Panchromatic Faint Object Counts for 0.2-2 μm Wavelength, 2011, XX.

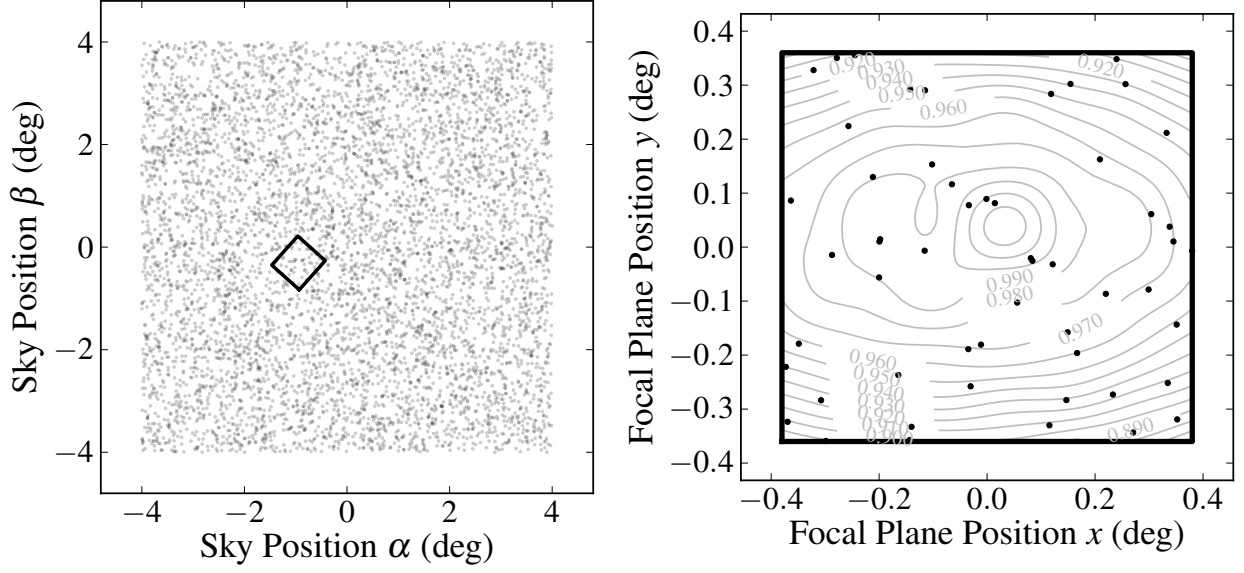


Fig. 1.— A single exposure of the synthetic sky. Left: A plot of the bright sources within the synthetic sky used in the self-calibration procedure, with the focal plane footprint overlaid. Right: The resultant distribution of the sources on the instrument’s focal plane. The *true* instrument model $f_{\text{true}}(\vec{x}_i|\vec{q}_{\text{true}})$ is shown with contours.

Table 1. A summary of the tuneable parameters in these simulations and their fiducial values.

Parameter	Fiducial Value
Source Density – Eqn. 1 (deg^{-2})	$a = -13.05, b = 1.25, c = -0.02$
Survey Area (deg^2)	8×8
Source Density (deg^{-2})	$d = 100$
Saturation Limit (mag)	$m_{\min} = 17$
10σ Detection Limit (mag)	$m_{\max} = 22$
Field-of-View (deg^2)	0.76×0.72
Noise Model – Eqn. 2	$\alpha = 0.1585, \eta = 0.0017, \epsilon_{\max} = 1.0$
Fitted Instrument Response Model	8 th order polynomial

Table 2. A summary of the four simple survey strategies considered in this paper.

Survey Label	Pointing Center	Orientation	Number of Pointings
A	Uniform Grid (12×12)	0°	1728
B	Uniform Grid (12×12)	Each Pass: $\theta + 30^\circ$	1728
C	Pass 1: Uniform Grid (12×12)	0°	1720
	Pass 2: Uniform Grid (13×11)		
	Pass 3: Uniform Grid (11×13)		
D	Quasi-Random	Random	1728

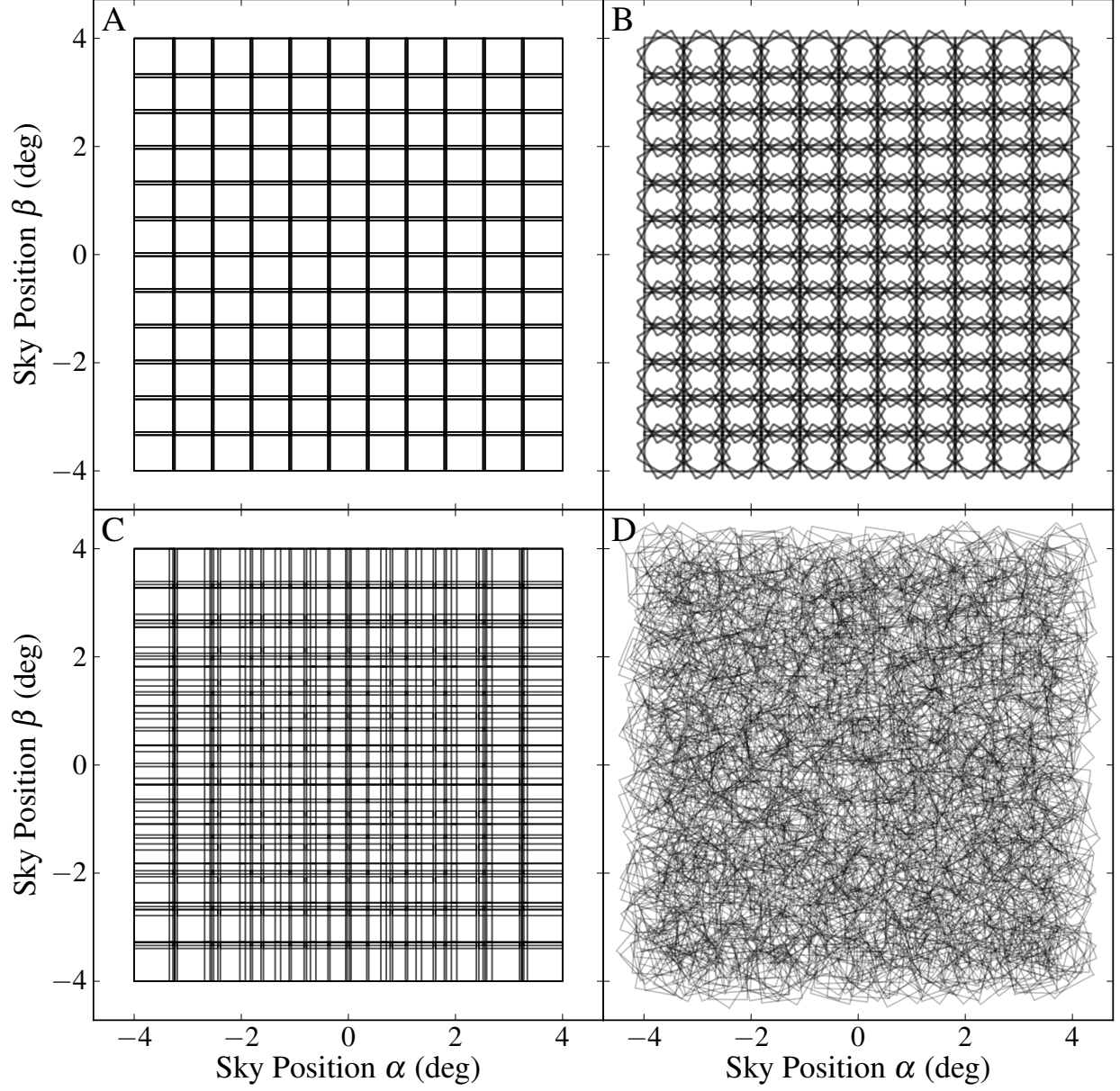


Fig. 2.— Focal plane footprints projected onto the synthetic sky according to the four simple survey strategies described in Section 5 and summarized in Table 2. Surveys A, B and D have 1728 pointings and survey C has 1720 pointings.

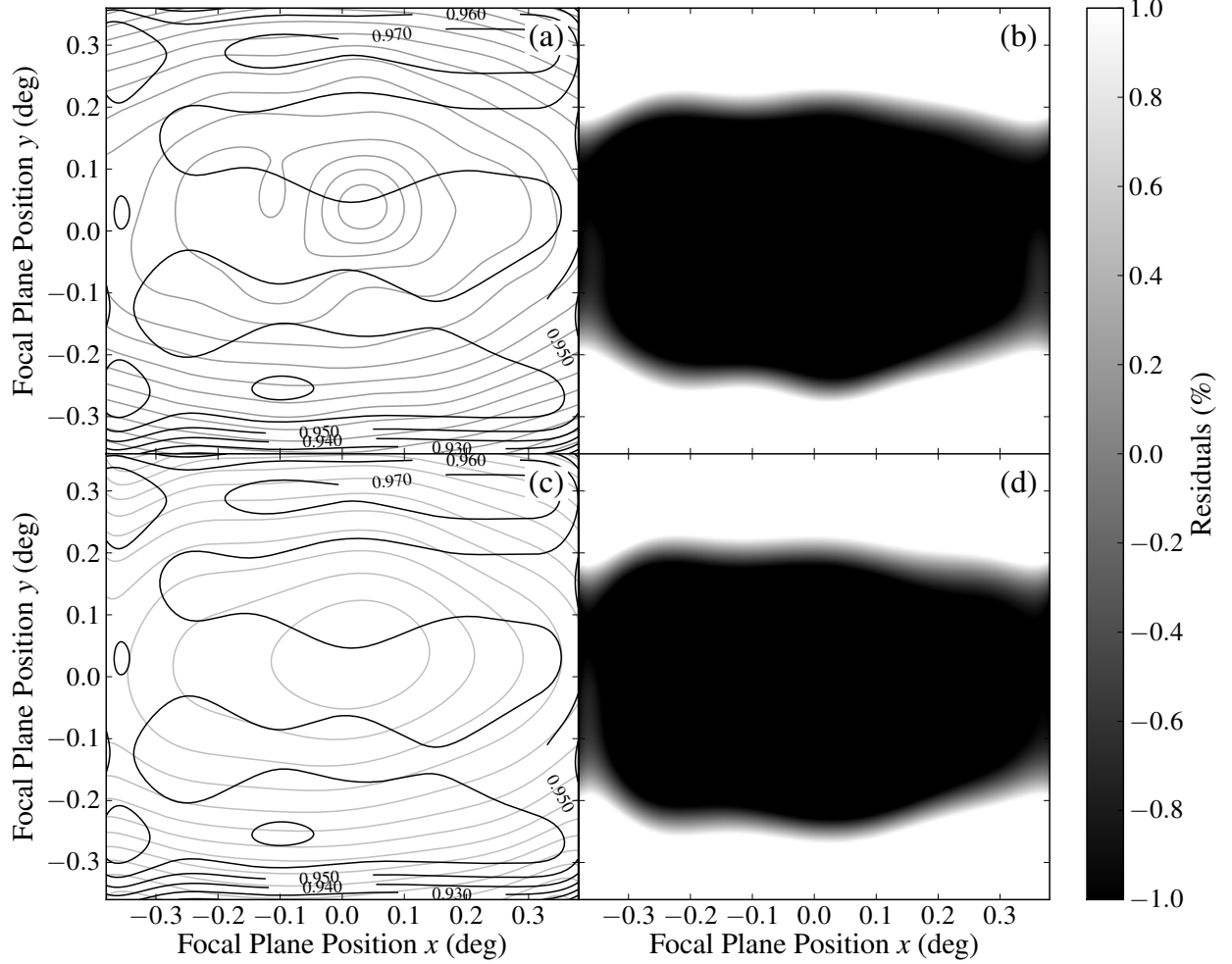


Fig. 3.— A comparison of the fitted instrument response model $f_{\text{fit}}(\vec{x}_j | \vec{q}_{\text{fit}})$ obtained from self-calibrating the Survey A dataset compared to the true $f_{\text{true}}(\vec{x} | \vec{q}_{\text{true}})$ and best-in-basis $f_{\text{best}}(\vec{x}_j | \vec{q}_{\text{best}})$ instrument response models. The self-calibration procedure did not converged to the final solution, the results presented here correspond to the instrument response found after 8192 iterations. (a) Contour plot of the fitted (black) compared to the *true* (gray) instrument response. (c) Contour plot of the fitted (black) compared to the *best-in-basis* (gray) instrument response model. The best-in-basis instrument response is the best fit to the true instrument response possible with the basis used to model the instrument response in the self-calibration procedure (in this case an eighth order polynomial). The plots (b) and (d) show the residuals between the two instrument response models plotted in (a) and (c) respectively.

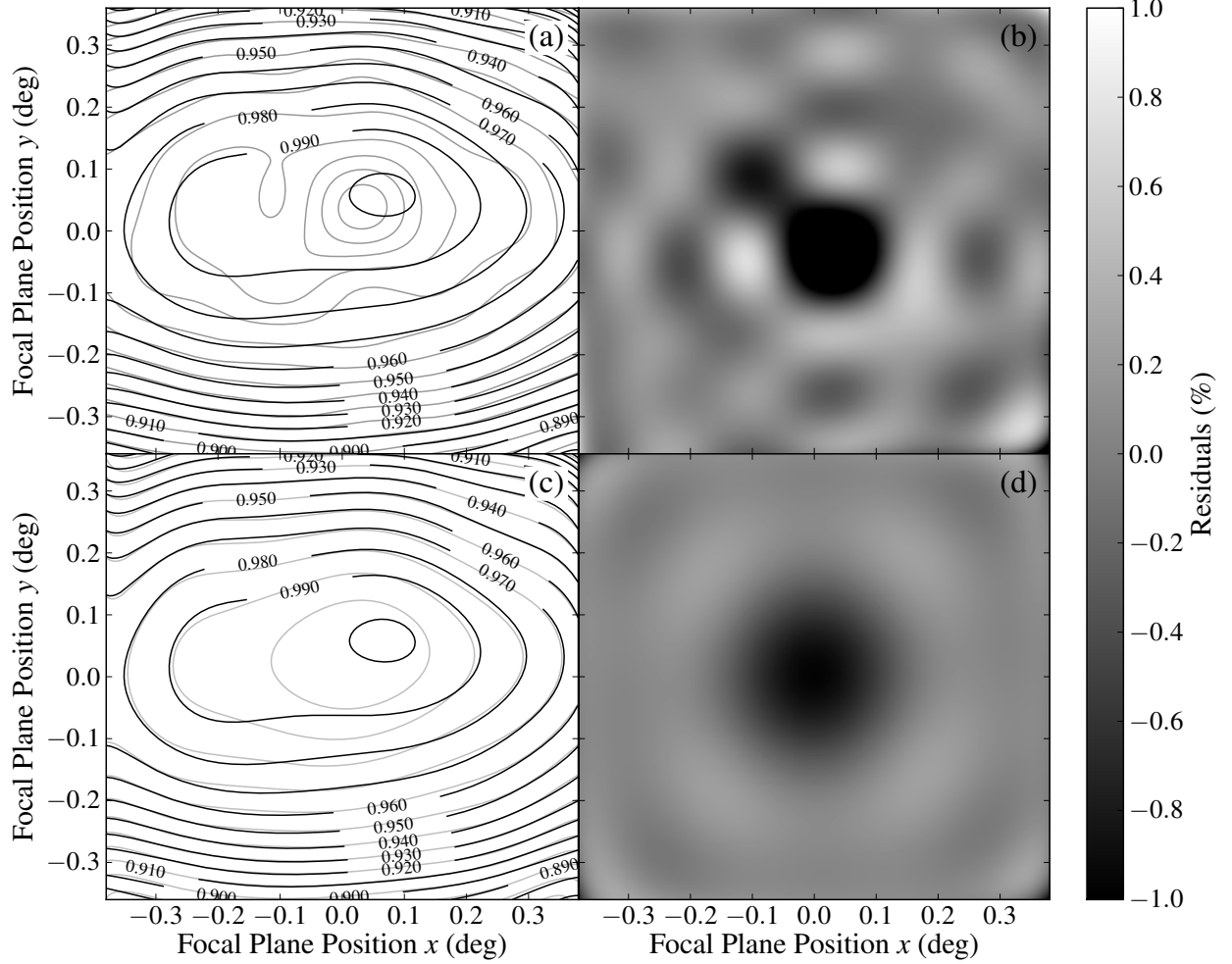


Fig. 4.— A comparison of the fitted instrument response model $f_{\text{fit}}(\vec{x}_j | \vec{q}_{\text{fit}})$ obtained from self-calibrating the Survey B dataset compared to the true $f_{\text{true}}(\vec{x} | \vec{q}_{\text{true}})$ and best-in-basis $f_{\text{best}}(\vec{x}_j | \vec{q}_{\text{best}})$ instrument response models. The self-calibration procedure converged to the final solution after 4160 iterations. (a) Contour plot of the fitted (black) compared to the *true* (gray) instrument response. (c) Contour plot of the fitted (black) compared to the *best-in-basis* (gray) instrument response model. The best-in-basis instrument response is the best fit to the true instrument response possible with the basis used to model the instrument response in the self-calibration procedure (in this case an eighth order polynomial). The plots (b) and (d) show the residuals between the two instrument response models plotted in (a) and (c) respectively.

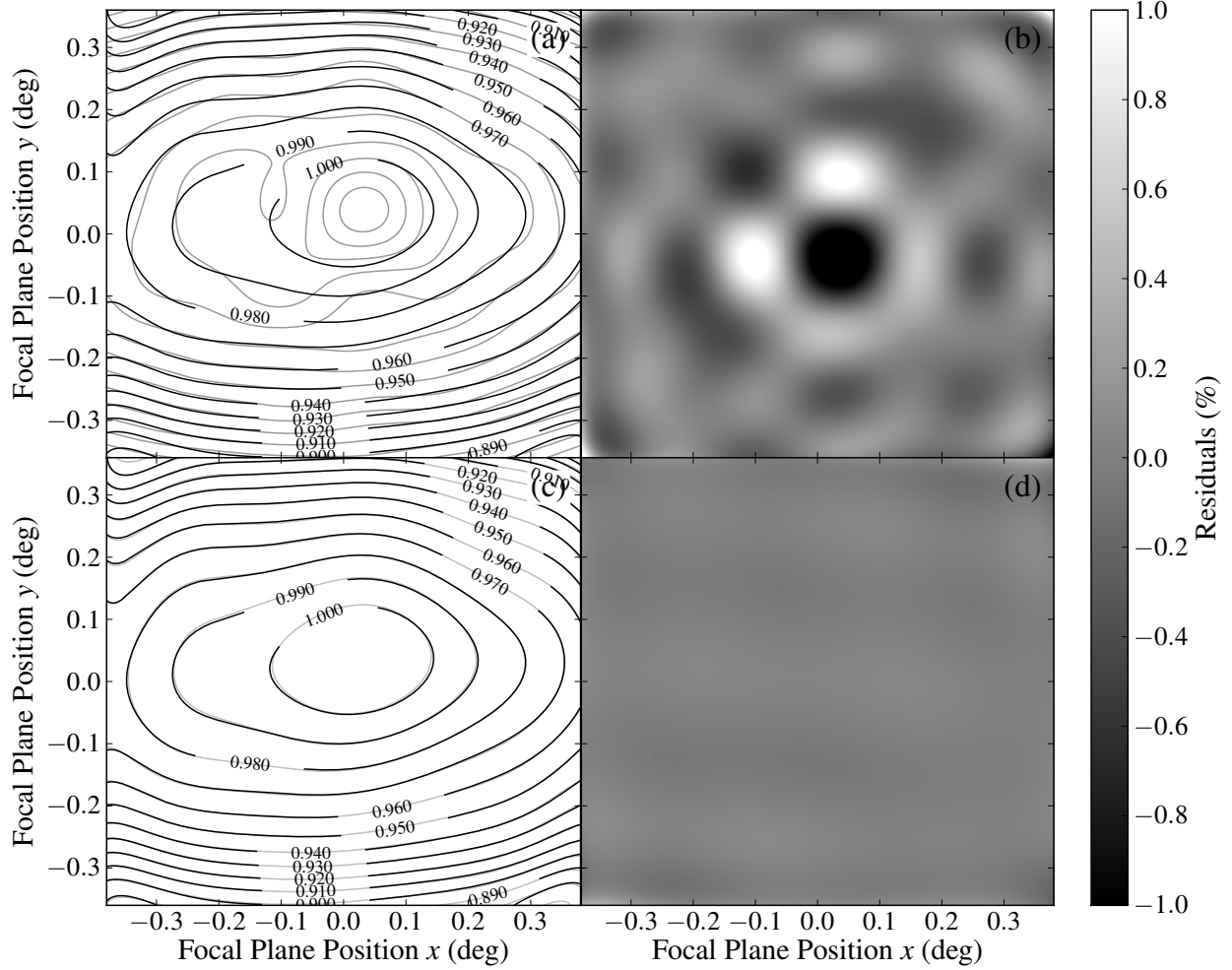


Fig. 5.— A comparison of the fitted instrument response model $f_{\text{fit}}(\vec{x}_j | \vec{q}_{\text{fit}})$ obtained from self-calibrating the Survey C dataset compared to the true $f_{\text{true}}(\vec{x} | \vec{q}_{\text{true}})$ and best-in-basis $f_{\text{best}}(\vec{x}_j | \vec{q}_{\text{best}})$ instrument response models. The self-calibration procedure converged to the final solution after 26 iterations. (a) Contour plot of the fitted (black) compared to the *true* (gray) instrument response. (c) Contour plot of the fitted (black) compared to the *best-in-basis* (gray) instrument response model. The best-in-basis instrument response is the best fit to the true instrument response possible with the basis used to model the instrument response in the self-calibration procedure (in this case an eighth order polynomial). The plots (b) and (d) show the residuals between the two instrument response models plotted in (a) and (c) respectively.

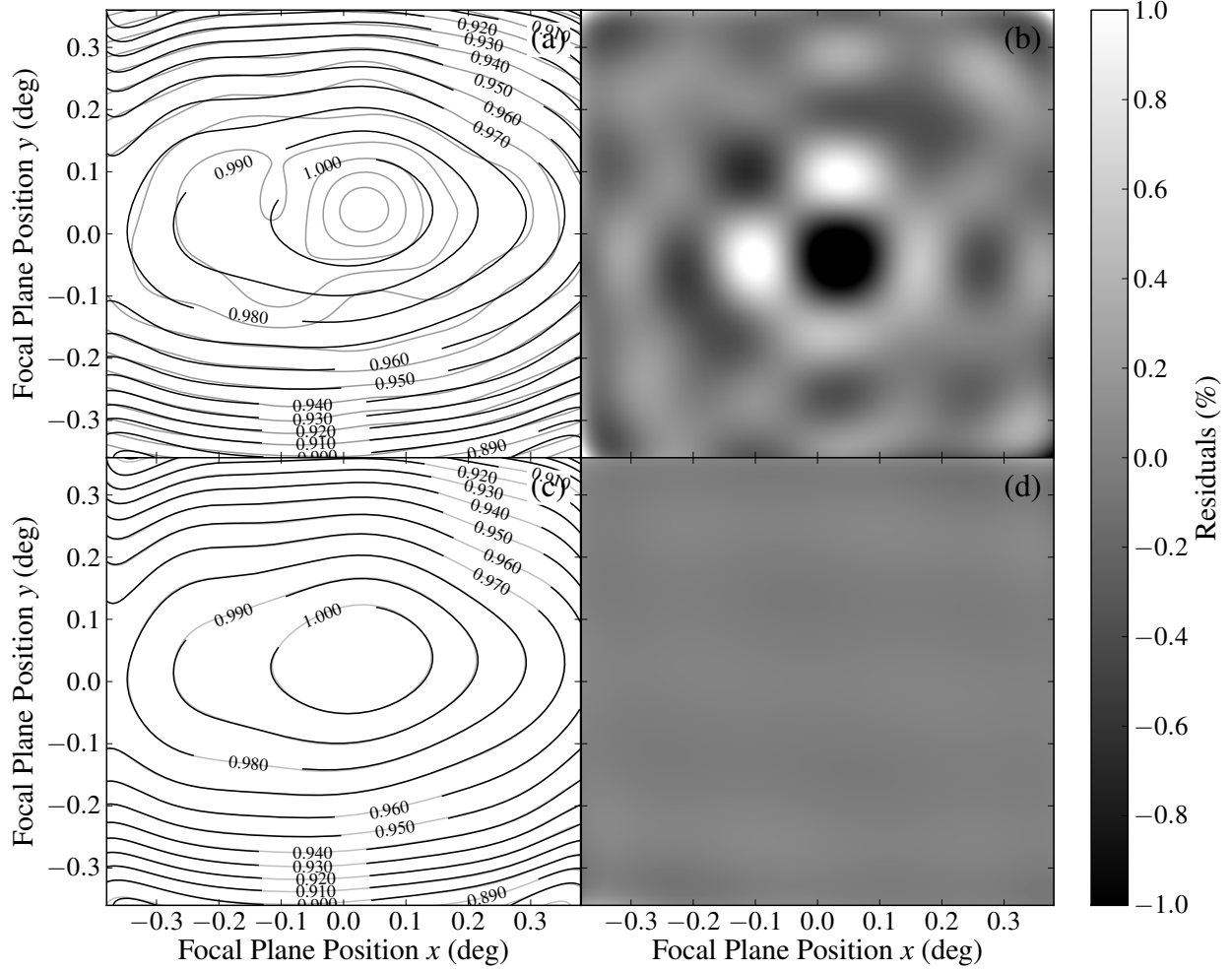


Fig. 6.— A comparison of the fitted instrument response model $f_{\text{fit}}(\vec{x}_j|\vec{q}_{\text{fit}})$ obtained from self-calibrating the Survey D dataset compared to the true $f_{\text{true}}(\vec{x}|\vec{q}_{\text{true}})$ and best-in-basis $f_{\text{best}}(\vec{x}_j|\vec{q}_{\text{best}})$ instrument response models. The self-calibration procedure converged to the final solution after 9 iterations. (a) Contour plot of the fitted (black) compared to the *true* (gray) instrument response. (c) Contour plot of the fitted (black) compared to the *best-in-basis* (gray) instrument response model. The best-in-basis instrument response is the best fit to the true instrument response possible with the basis used to model the instrument response in the self-calibration procedure (in this case an eighth order polynomial). The plots (b) and (d) show the residuals between the two instrument response models plotted in (a) and (c) respectively.

Table 3. A summary of the quality of the final fit from the self-calibration procedure with the four simple survey strategies summarized in Table 2. The self-calibration procedure was run with only the brightest sources within the survey area; the source error S_{RMS} corresponds to the measurements of these sources only and not all those within the survey.

*Did not converge.

Survey Name	Iterations	Source Error $S_{\text{RMS}}(\%)$	True Badness $B_{\text{true}} (\%)$	Best-in-Basis Badness $B_{\text{BIB}} (\%)$
A*	8192	XX	XX	XX
B	4160	XX	XX	XX
C	26	0.199	0.305	0.043
D	9	0.113	0.304	0.032